Journal of Medicinal Chemistry

Article

pubs.acs.org/jmc

Novel Pyridazinone Inhibitors for Vascular Adhesion Protein-1 (VAP-1): Old Target–New Inhibition Mode

Eva Bligt-Lindén,[†] Marjo Pihlavisto,[‡] István Szatmári,[§] Zbyszek Otwinowski,[∥] David J. Smith,[‡] László Lázár,[§] Ferenc Fülöp,[§] and Tiina A. Salminen*[,†]

[†]Structural Bioinformatics Laboratory, Department of Biosciences, Åbo Akademi University, FI-20520 Turku, Finland

[‡]Biotie Therapies Corporation, FI-20520 Turku, Finland

[§]Institute of Pharmaceutical Chemistry and Stereochemistry Research Group of Hungarian Academy of Sciences, University of Szeged, Eötvös u. 6, H-6720 Szeged, Hungary

[∥]Otwinowski Laboratory, Department of Biophysics and Department of Biochemistry, UT Southwestern Medical Center, Dallas, Texas 75390-8816, United States

Supporting Information

ABSTRACT: Vascular adhesion protein-1 (VAP-1) is a primary amine oxidase and a drug target for inflammatory and vascular diseases. Despite extensive attempts to develop potent, specific, and reversible inhibitors of its enzyme activity, the task has proven challenging. Here we report the synthesis, inhibitory activity, and molecular binding mode of novel pyridazinone inhibitors, which show specificity for VAP-1 over monoamine and diamine oxidases. The crystal structures of three inhibitor–VAP-1 complexes show that these compounds bind reversibly into a unique binding site in the active site channel. Although they are good inhibitors of human VAP-1, they do not inhibit rodent VAP-1 well. To investigate this further, we used homology modeling and structural comparison to identify amino acid differences, which explain the species-specific binding properties. Our results prove the potency and specificity of these new inhibitors, and the detailed characterization of their binding mode is of importance for further development of VAP-1 inhibitors.

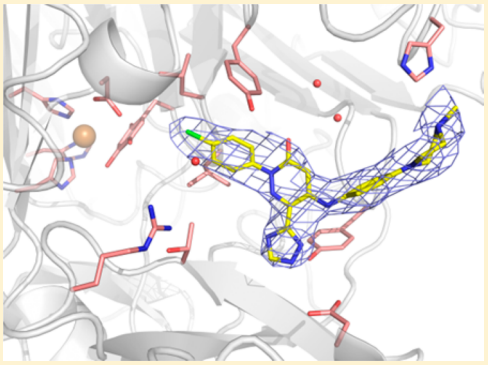

INTRODUCTION

Human primary amine oxidase (AOC3), also known as vascular adhesion protein-1 (VAP-1) or semicarbazide-sensitive amine oxidase (SSAO), has been investigated as a potential drug target of inflammatory diseases because of its involvement in leukocyte trafficking. To date, inhibitors of SSAO have targeted the active site topaquinone (TPQ) cofactor and the mode of inhibition has been irreversible, or slowly reversible, and the recovery of enzyme activity is thus a consequence of new enzyme synthesis.[1] This is an undesirable characteristic for a drug for human use where the ability to remove drug and regain target activity within a short period of time is important. Here we have synthesized a series of novel pyridazinone VAP-1 inhibitors, which show a reversible binding mode.

VAP-1 belongs to the family of copper-containing amine oxidase/semicarbazide-sensitive amine oxidase (CAO/SSAO) enzymes. It is a membrane-bound glycoprotein, which enzymatically converts primary amines to the corresponding aldehydes in a reaction where hydrogen peroxide and ammonia are produced: $RCH_2NH_2 + H_2O + O_2 \rightarrow RCHO + H_2O_2 + NH_3$.[2] Benzylamine and methylamine are the preferred substrates for VAP-1 in vitro,[3] but its physiological substrate is still uncertain. Methylamine and aminoacetone produced as side products of intermediary metabolism in man could serve as in vivo substrates and enhance cell adhesion by facilitating hydrogen peroxide production.[4] Additionally, VAP-1 binds Siglec-9 and Siglec-10, which are leukocyte-surface proteins.[5] Through the adhesive functions, VAP-1 is involved in leukocyte trafficking to sites of inflammation, which makes it a potential drug target to treat acute and chronic inflammatory conditions like rheumatoid arthritis, psoriasis, atopic eczema, multiple sclerosis, diabetes, and respiratory diseases.[6] Additionally, VAP-1 has been proposed to have roles in diabetic vascular disease and fibrosis.

The CAO crystal structures from many organisms have been determined: eubacteria (*Escherichia coli*[7] and *Arthrobacter globiformis*[8]), yeast (*Hansenula polymorpha*[9] and *Pichia pastoris*[10]), fungi (*Aspergillus nidulans*[11]), plants (*Pisum sativum*[12]), and mammals (*Homo sapiens*[13−15] and *Bos taurus*[16,17]). The CAOs are all tightly bound homodimers with a similar 3D structure, consisting of a D2, a D3, and a catalytic D4 domain. The buried active site is highly conserved and has several common features: the TPQ and a conserved aspartic acid residue (Asp386) are both involved in the catalytic reaction, and three conserved histidines (His520, His522, His684) coordinate the copper ion involved in TPQ biogenesis.[2]

Received: June 26, 2013
Published: December 4, 2013

Scheme 1. Synthesis of 5-Cyclohexylamino- (6) and 5-Isopropylamino-2-phenyl-6-(1*H*-1,2,4-triazol-5-yl)-3(2*H*)-pyridazinones[a]

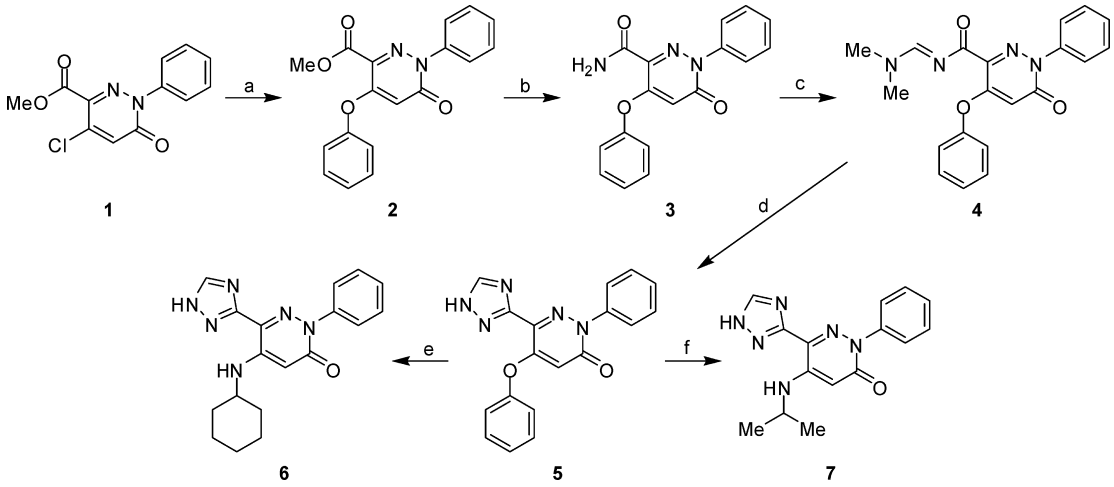

[a]Reagents and conditions: (a) $PhONa{\cdot}3H_2O$, DMF, rt, 24 h, 72%; (b) NH_3, MeOH, rt, 45 min, 83%; (c) $(MeO)_2CHNMe_2$, 90 °C, 15 min, 84%; (d) $H_2N\text{-}NH_2{\cdot}H_2O$, 90 °C, 1.5 h 89%; (e) cyclohexylamine, 140 °C, 3 h, 77%; (f) Me_2CHNH_2, microwave, 150 °C, 1 h, 76%.

Several approaches to inhibit VAP-1 have been discussed in the literature.[6] Function blocking antibodies, small interfering RNAs, and small molecule inhibitors have been shown to be effective. The most studied group of inhibitors are the small molecules, including hydrazines, compounds with thiazole or another nitrogen-containing heterocyclic core, allylamines, amino acid derivatives, benzamides, oxime-based SSAO-inhibitors, aminoglycoside antibiotics, vitamin B1 derivatives, and peptides.[6] The first crystal structure of human VAP-1 in complex with an irreversible inhibitor 2-hydrazinopyridine (2HP) was solved in 2005 by Jakobsson and co-workers,[14] and so far it has been the only structure of a human VAP-1−inhibitor complex.

New structures of human VAP-1 in complex with imidazole molecules presented a secondary imidazole binding site in the active site channel.[18] This raised the idea that the active site channel may provide a new target area for drug design for human VAP-1 inhibitors, which has thereafter been discussed by Bonaiuto and co-workers in relation to synthetic polyamines.[19] Instead of utilizing an irreversible inhibitor that would covalently bind to the active site TPQ, we have designed, synthesized, and crystallized a series of reversible pyridazinone inhibitors that bind in the active site channel instead of binding to TPQ or its vicinity. We have also tested the in vitro activity of the inhibitors toward human, cynomolgus monkey, and mouse VAP-1s. Similar to many other VAP-1 ligands,[20−22] the pyridazinone inhibitors were shown to have species-specific binding properties. To analyze the 3D structure of the inhibitor binding site in rodent and primate VAP-1s, we made homology models for the inhibitor complexes of mouse, rat, and cynomolgus monkey VAP-1. By comparing the X-ray structures and homology models, we could pinpoint residues that cause these structural and functional differences between rodent and primate VAP-1s, which are important to understand as rodents often are used in the in vivo testing of drugs. The identified residues are scattered all over the active site channel, which would make the design of pyridazone inhibitors binding equally well to rodent and primate VAP-1 very challenging. Further development of these pyridazinone compounds will continue, but it will require the use of human VAP-1 transgenic mice or nonhuman primates as model species. In general, our results provide valuable information which should be considered when reversible inhibitors are targeted to the active site cavity of human VAP-1.

RESULTS AND DISCUSSION

Syntheses. For the synthesis of the desired 5-substituted pyridazinone derivatives, the starting halogenoderivatives **1**[23] and **8**[24] were prepared according to literature procedures.

The coupling of **1** with sodium-phenolate at room temperature led to **2**,[25] the amidation of which by methanolic ammonia solution resulted in the corresponding carboxamide **3**. A two-step conversion[26] amide **3** with *N*,*N*-dimethylformamide dimethyl acetal, followed by the treatment of the intermediate **4** with hydrazine hydrate in acetic acid gave 5-phenoxy-2-phenyl-6-(1*H*-1,2,4-triazol-3-yl)-3(2*H*)-pyridazinone (**5**). The nucleophilic substitution of the enolether group of **5** by cyclohexylamine, or isopropylamine, led to the 5-aminoalkyl-substituted pyridazinone derivatives **6** and **7**, respectively (Scheme 1).

To increase the water solubility by inserting piperazine into the molecule, the synthesis of 5-(4-(4-methylpiperazin-1-yl)-phenylamino)-substituted pyridazinone derivative (**13**) was also accomplished. The coupling reaction[27,28] between the chloro derivative **8** and 4-(4-methylpiperazin-1-yl)aniline (**9**)[29] gave enamine **10**, the ester group of which was transformed to amide (**11**) by using methanolic ammonia solution. The carboxamide triazole transformation was performed via the formamidine derivative **12**. The treatment of **12** with hydrazine hydrate resulted in compound **13**, which was isolated as a monohydrochloride salt (Scheme 2).

In Vitro Inhibitory Activity of the VAP-1 Inhibitors. The in vitro inhibitory activity of novel 5-substituted pyridazinone inhibitors **6**, **7**, and **13** were tested using recombinant VAP-1. The results indicate that the novel VAP-1 inhibitor compounds are very potent against human VAP-1 enzyme activity, having IC_{50} values from 290 to 20 nM. These inhibitors are very specific for human over mouse VAP-1 because they are very weak inhibitors of mouse VAP-1 activity (Table 1 and Figure 1). The data with other rodent species like rat, guinea pig, and hamster also shows lack of inhibition against rodent VAP-1 (data not shown). On the contrary, the potency against VAP-1 of another primate, cynomolgus monkey, is very similar to human VAP-1 with

dx.doi.org/10.1021/jm401372d | J. Med. Chem. 2013, 56, 9837−9848

Scheme 2. Synthesis of 5-[4-(4-Methylpiperazin-1-yl)phenylamino]-2-(4-chlorophenyl)-6-(1*H*-1,2,4-triazol-5-yl)-3(2*H*)-pyridazinone Hydrochloride[a]

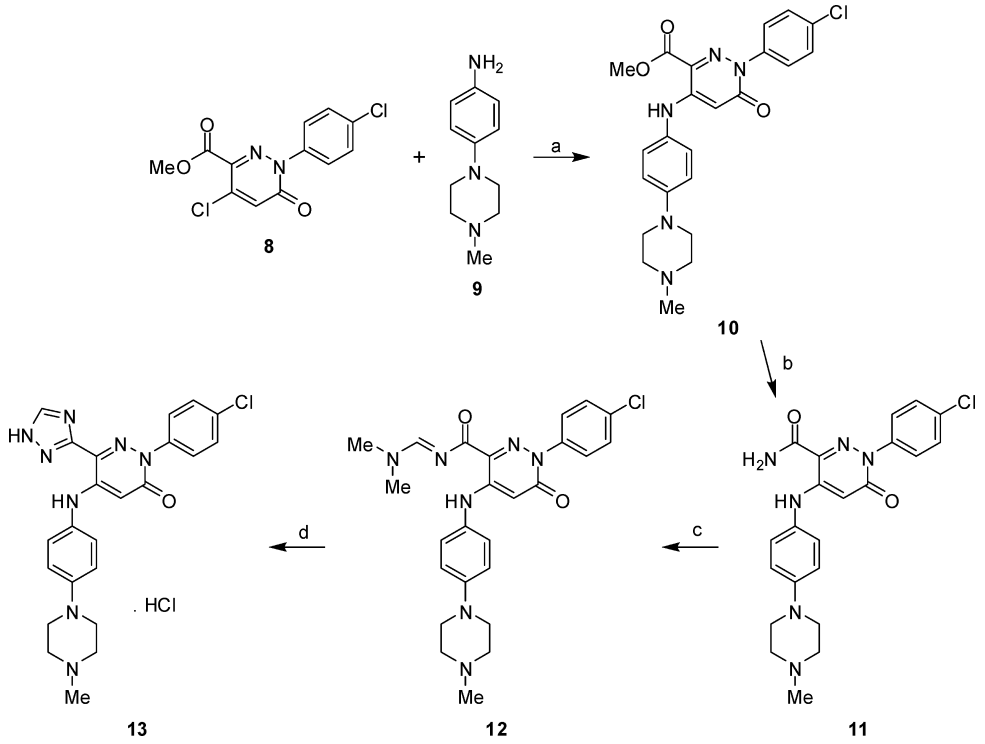

[a]Reagents and conditions: (a) EtOH, reflux, 30 h, 75%; (b) NH_3, MeOH, rt, overnight, 92%; (c) $(MeO)_2CHNMe_2$, 80 °C, 10 min, 93%; (d) (1) H_2N-NH_2·H_2O, 80 °C, 1.5 h, (2) HCl, EtOH.

Table 1. In Vitro Potency and Specificity of the Novel VAP-1 Inhibitor Compounds

compd	hVAP-1[a] IC_{50} (μM)	mVAP-1[b] % inhib	cVAP-1[c] IC_{50} (μM) at 20 μM	tMAO/$hMAO_A$/$hMAO_B$[d] % inhib at 100/20/20 μM	DAO[e] % inhib at 50 or 100 μM
6	0.071 ± 0.007	24 ± 8	0.13 ± 0.02	3 ± 2/4 ± 2/13 ± 3	40 ± 6 at 100 μM
7	0.29 ± 0.06	10 ± 3	0.25 ± 0.03	8 ± 2/nd/nd	30 ± 10 at 100 μM
13	0.020 ± 0.002	23 ± 3	0.026 ± 0.01	18 ± 5/3 ± 1/1 ± 1	36 ± 3 at 50 μM

[a]Recombinant human VAP-1 purified protein. [b]Recombinant mouse cell lysate of VAP-1 protein. [c]Recombinant cynomolgus cell lysate of VAP-1 protein. [d]tMAO extracted from rat liver (total rat monoamine oxidase A and B); recombinant human MAO_A and MAO_B (human monoamine oxidase A and B) expressed in baculovirus infected BTI insect cells (Sigma). [e]DAO (diamine oxidase from porcine kidney). The results are the mean of two to six experiments ± SE or one representative inhibition percent when the calculation of the confidential IC_{50} values impossible. nd = not determined.

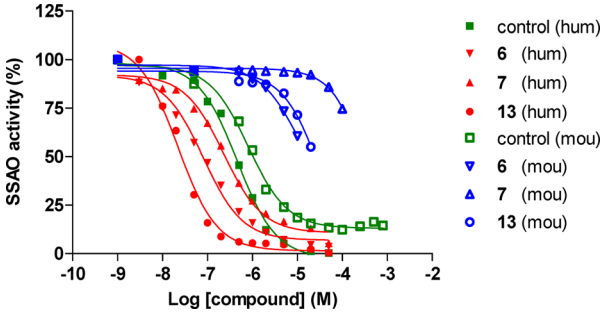

Figure 1. One representative curve of each compound illustrating the human VAP-1 specific inhibition activity (red) of compounds **6**, **7**, and **13** against mouse VAP-1 activity (blue). A control compound is equally effective for both species (green). The control compound is (1*S*,2*R*)-2-(1-methylhydrazino)-1,2-diphenylethanol (*S*,*S*)-tartrate salt as previously reported.[30]

compounds **6**, **7**, and **13**. The hydrazine derived inhibitor (1*S*,2*R*)-2-(1-methylhydrazino)-1,2-diphenylethanol (*S*,*S*)-tartrate salt (**11d**)[30] that has been shown to bind irreversibly to the TPQ was used as a control and it inhibits the VAP-1 of both human and rodent species.

Inhibitor **13** is the most potent human VAP-1 inhibitor out of these three novel inhibitors, with a IC_{50} value of 20 nM, while inhibitor **7** has the lowest activity toward human VAP-1, with a IC_{50} value of 290 nM. The binding kinetics of compounds **6** and **7** to human VAP-1 immobilized on a chip were also determined using Biacore surface plasmon resonance analysis and demonstrate a high affinity binding (K_D = 0.17 × 10^{-6} M for **6** and K_D = 0.20 × 10^{-6} M for **7**) with very fast association kinetics (k_a = 1.00 × 10^{-6} M^{-1} s^{-1} for **6** and k_a = 1.88 × 10^{-6} M^{-1} s^{-1} for **7**) and moderate dissociation kinetics (k_d = 0.17 × 10^{-6} s^{-1} for **6** and k_d = 0.38 × 10^{-6} for **7**) for both of them. Inhibitors **6** and **13** show similar potency toward mouse VAP-1, and again inhibitor **7** shows the lowest activity (Table 1 and Figure 1). We, and others, have previously predicted that the smaller channel and different cavity shape of rodent VAP-1 proteins compared to human VAP-1 protein[31,32] can account for the difference in the in

dx.doi.org/10.1021/jm401372d | *J. Med. Chem.* 2013, 56, 9837−9848

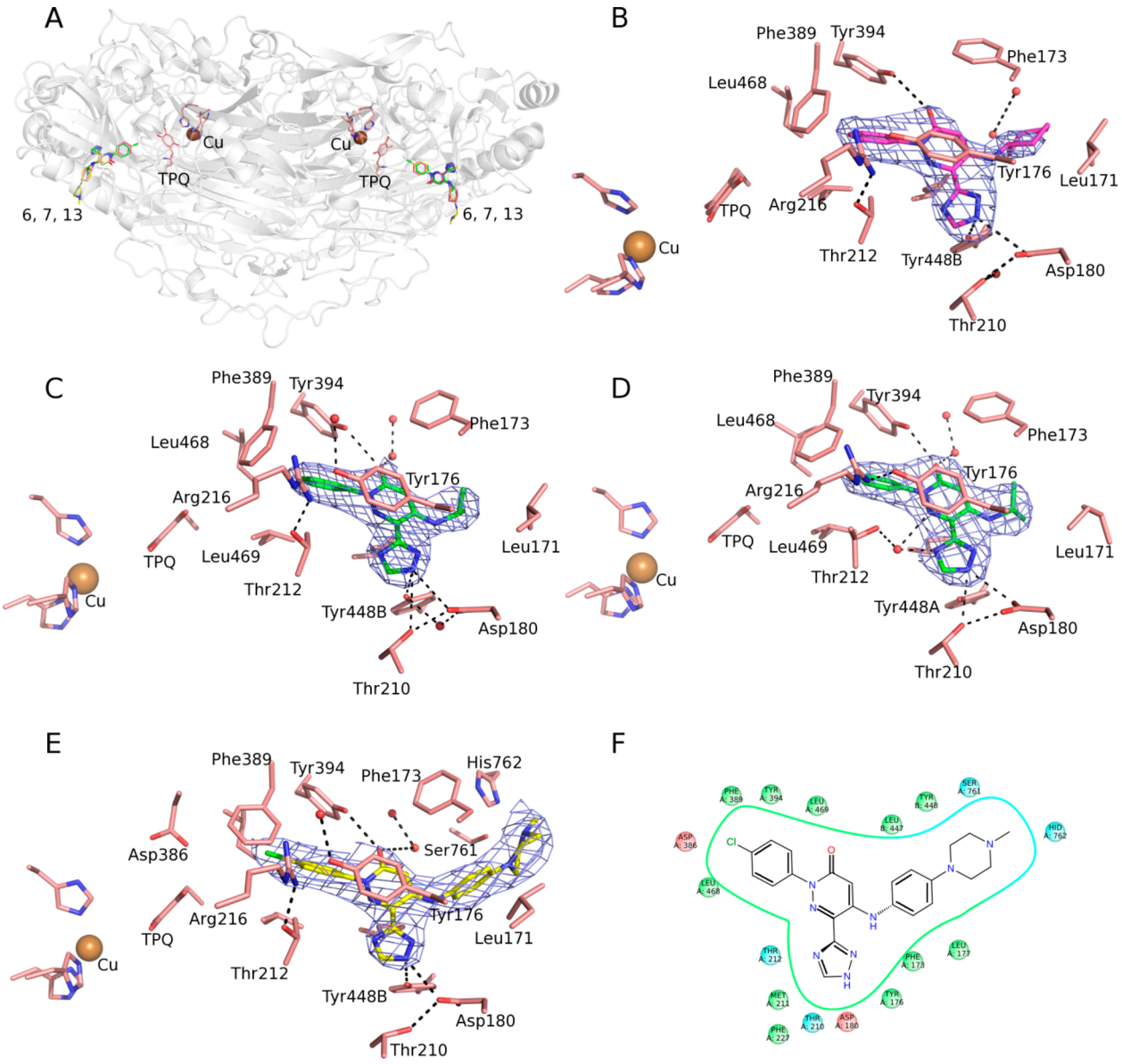

Figure 2. Molecular binding mode for inhibitors **6**, **7**, and **13** in human VAP-1. (A) Overall view of the VAP-1 inhibitor complexes. Inhibitors **6**, **7**, and **13** are bound in the active site channel, close to the previously reported secondary imidazole binding site, and they are shown as magenta, green, and yellow sticks, respectively. VAP-1 residues, including TPQ, are shown as salmon sticks, and copper ions are shown as brown spheres. (B) Binding mode for inhibitor **6** (shown as magenta sticks) in chain A of VAP-1. (C) Binding mode of **7** (shown as green sticks) in chain A of VAP-1, where Thr212 makes a hydrogen bond to Arg216. (D) Binding mode of **7** (shown as green sticks) in chain B of VAP-1, where Thr212 is involved in a water-mediated hydrogen bond to the ligand. (E) Binding mode of **13** (shown as yellow sticks) in chain A of VAP-1. (F) 2D plot of residues within 5 Å of inhibitor **13** bound in VAP-1. The σ level of the $2F_o - F_c$ electron density maps are contoured at 1.5 in C–E and at 1.0 in B. The electron density maps are calculated for the whole structure but only the densities for the inhibitors are shown.

vitro inhibitor binding properties of these species, where primate VAP-1 prefers bulkier and more hydrophobic ligands than rodent VAP-1.[31] This binding data supports the hypothesis, as the largest and most hydrophobic ligand, inhibitor **13**, shows the best binding. The second phenyl ring and the piperazine group of **13** accounts for its better binding because the lack of these groups in **7** leads to lower potency. Overall, the inhibitors are rather hydrophobic, which leads to better binding in human than in mouse VAP-1. These compounds also have excellent specificity for VAP-1 over monoamine and diamine oxidases (MAO and DAO), which is not surprising due to the structural differences between these novel inhibitors with respect to inhibitors designed for MAO and DAO. Total rat MAO inhibition, including both monoamine A and B isoforms, is only 3–18% at 100 μM concentrations. The corresponding inhibition data for **6** and **13** was also determined with purified human MAO A and MAO B isoforms and gave similar results (Table 1).

As these pyridazinones are good human VAP-1 inhibitors while being poor versus the mouse homologue, other methods than in vivo rodent testing are worth considering for future studies. Suitable approaches would include the use of transgenic mice expressing human VAP-1 for in vivo models, further use of in vitro or ex vivo human disease models and using nonhuman primates for toxicological studies, or, where suitable disease models exist, for in vivo efficacy studies.[33−35]

dx.doi.org/10.1021/jm401372d | J. Med. Chem. 2013, 56, 9837−9848

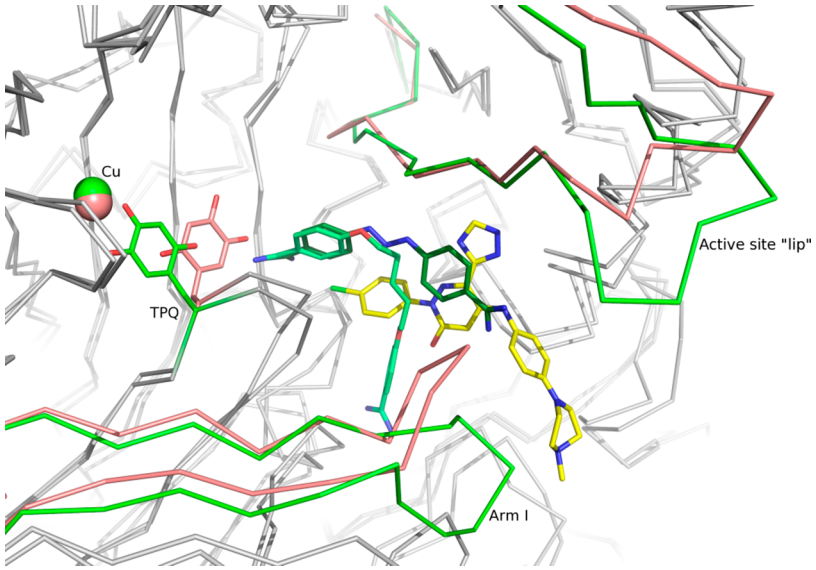

Figure 3. Comparison of the inhibitor bound complexes of DAO and VAP-1. The arm I and upper active site "lip" of **13**–VAP-1 structure (salmon) and DAO complexes (green) (PDB codes 3HIG and 3HII[40]) are shown as ribbons, and the rest of the proteins are shown as gray ribbons. **13** is shown in yellow sticks, berenil in forest green sticks and pentamidine in pale-green sticks. TPQ and Cu are shown as sticks and spheres, respectively.

Structural Studies. *Crystal Structures of the Inhibitor–VAP-1 Complexes.* To study the binding site and mode of the inhibitors at atomic level, we determined the crystal structures of inhibitors **6**, **7**, and **13** in complex with human serum VAP-1. The structures were refined to 2.80, 2.78, and 3.10 Å resolution, respectively. The *R*-factors for the three different structures are 20.5%, 17.4%, and 18.5%, with an *R*-free of 26.0%, 23.6%, and 25.0%, respectively. Despite the very anisotropic data sets, the electron density is good throughout the structures (Supporting Information Figure 2A,B). All structures contain a homodimer in the asymmetric unit, and monomers A and B are related by the 2-fold noncrystallographic axes. The monomers are comprised of three domains (D2, D3, and D4) similar to the other reported CAO structures.[2] The D4 domain forms the intermonomeric interface, and it has the deeply buried active site, which is accessed through a narrow and 15 Å long channel. The D2 and D3 domains surround the central D4 dimer. Tyr471 is post-translationally modified to TPQ, and it is in the active, off-copper conformation in all the chains of the complex structures. One copper ion and two calcium ions are bound to each subunit. VAP-1 is extensively glycosylated with carbohydrates bound at four or five of the six N-linked glycosylation sites[13,36] in each monomer, and there is good electron density to model the oligosaccharide chains to all previously identified sites (Supporting Information Figure 2C).

The binding mode of these novel inhibitors significantly differs from the complex structure of human VAP-1 and 2HP.[14] The binding mode is also different from all recent computational studies, where docking and QSAR models of potential VAP-1 inhibitors have been published.[19,20,30,37−39] Unlike 2HP, which binds covalently to TPQ,[14] the molecules **6**, **7**, and **13** bind noncovalently in the channel leading to the active site. These novel inhibitors block the entrance and hinder any ligand of entering the active site (Figure 2). The binding site is distinct but close to the position that was named as the secondary imidazole binding site in our previously published VAP-1 structures.[18]

Comparison of the inhibitor bound structures with the previously determined native structure of VAP-1 (PDB code 1US1[13]) shows that the structures are almost identical, with the exception of the conformation of two residues (Phe173 and Phe389) in the active site channel. In the inhibitor bound structures, Phe173 has taken an alternative conformation to allow passage and create additional space for the inhibitors to bind. Compared to the native (PDB code 1US1[13]) and imidazole bound structures (PDB codes 2Y73 and 2Y74[18]), the phenyl ring of Phe389 interacts with all inhibitors and it is slightly rotated to make more favorable interactions to molecules **6** and **7**. Root-mean-square differences (rmsd) after superposition of **6**, **7**, and **13** bound structures to the native structure are 0.40 Å (1339 atoms), 0.28 Å (1282 atoms), and 0.32 Å (1299 atoms), respectively. Similarly, there were not many differences to the native structure in the two previously published inhibitor complex structures of human DAO.[40]

The $2F_o - F_c$ density map for the inhibitors is good and the inhibitors could easily be modeled in all chains (Figure 2B–E). The omit maps (Supporting Information Figure 2D–F) and $F_o - F_c$ maps (Supporting Information Figure 3A–C) for the ligands further verifies their location. However, electron density for the cyclohexyl of inhibitor **6** is partly missing due to its flexible nature and the fact that it is solvent exposed. Because of the similar scaffold, the inhibitors bind in a similar way through hydrogen bonds, π-stacking, and hydrophobic interactions, with some minor differences (Figure 2B–E). Tyr394, Asp180, and Thr210 form hydrogen bonds to all the inhibitors. Tyr176 π-stacks to the pyridazinone and the hydroxyl group of Tyr448 on arm I originating from the other monomer makes a hydrogen bond with the nitrogen in the triazole ring of the inhibitors in all chains of all structures. Additionally, Phe389 makes a T-shaped π-stacking with the phenyl ring of inhibitors **6** and **7**, as well as a Cl–π interaction with inhibitor **13**. Furthermore, Phe173, Leu177, Leu468, and Leu469 interact hydrophobically with the inhibitors. In all B chains, the side chain of Thr212 hydrogen bonds through a water molecule to the ligands (Figure 2D) and Arg216 is involved in a hydrogen bond with Tyr176. However, Thr212 in all A chains is flipped 180° and does not interact with the inhibitors (Figure 2B,C,E) but instead forms a hydrogen bond with Arg216. Similarly, in the human VAP-1 imidazole complex structure (PDB code 2Y73[18]),

dx.doi.org/10.1021/jm401372d | *J. Med. Chem.* 2013, 56, 9837–9848

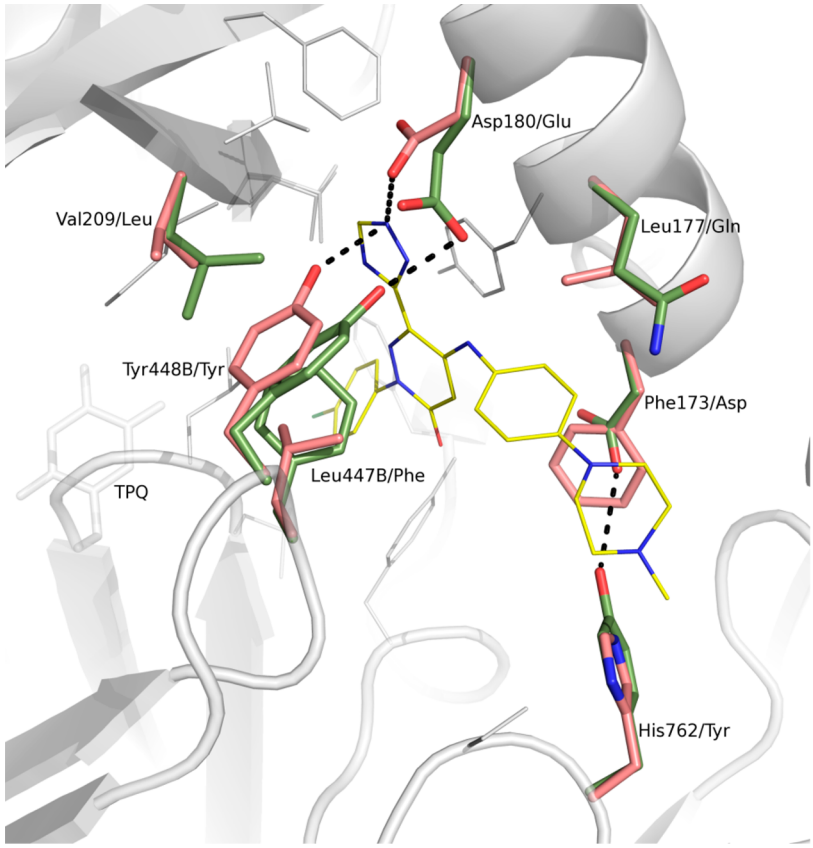

Figure 4. Differences in the active site channel of human and mouse VAP-1 in chain A. The residues that differ between the species are shown as sticks; human residues in salmon and mouse residues in green. The carbon atoms of inhibitor **13** are shown as yellow lines. Tyr448B and Glu180 are hydrogen bonded in the mouse protein, while Tyr448B and Asp180 in the human protein are hydrogen bonding to the inhibitor. Additionally, Tyr762 and Asp173 in the mouse VAP-1 model are hydrogen bonded to each other.

Thr212 interacted with Arg216 in one chain, but in the other chain a water molecule mediated its interaction with the imidazole. In both **7** and **13** bound complexes, the oxygen atom of the pyridazinone interacts with a water molecule (Figure 2C,D,E).

There are currently only four crystal structures available where inhibitors are bound to mammalian CAOs: hVAP−2HP complex,[14] BSAO in complex with clonidine,[17] and DAO in complex with berenil and pentamidine.[40] These novel pyridazinone inhibitors of VAP-1 all bind noncovalently, similarly to clonidine, berenil, and pentamidine. The superposition of the compound **13**−VAP-1 complex to the hDAO complexes shows that the pyridazinone inhibitors bind closer to the opening of the channel than berenil and pentamidine (Figure 3). In the hDAO structures, the TPQ is in on-copper inactive conformation, while in the **6**, **7**, and **13** complexes, it is in off-copper active position (Figure 3). The closest point of contact to TPQ is 4.5 Å in berenil−hDAO complex structure and 4.0 Å in pentamidine−hDAO complex, but in the pyridazinone−VAP-1 complexes the corresponding distance is clearly longer (6.5 Å in **6**, 6.9 Å in **7**, and 6.1 Å in **13**). The structural differences in the active site opening, including arm I from the other monomer, make the entrance to the active site channel narrower in DAO than in VAP-1, which might affect the ligand binding properties[40] (Figure 3).

Molecular Modeling. In our recently published structural comparison of the active site channels of primate and rodent VAP-1, we identified several amino acid substitutions that might cause species-specific differences in ligand binding to human, cynomolgus monkey, rat, and mouse VAP-1. Sequence comparisons, together with structural comparisons of the crystal structure of native human VAP-1 and the homology models of mouse, rat, and monkey VAP-1, showed that the substitutions at positions 173, 177, 180, 210, 761, and 762 in one monomer and 447 in the other monomer, all lay right at the entrance, or in, the active site channel.[31] Here we have made models of mouse and cynomolgus monkey VAP-1 based on the VAP-1−**13** complex to explain the species-specific binding of the **6**, **7**, and **13** molecules. The only difference between the human and the cynomolgus VAP-1 is that Thr212 in human VAP-1 is substituted with Asn in the cynomolgus protein, which does not give rise to large differences in the activity of inhibitors toward these proteins. However, there are several differences between the human and mouse protein in the active site channel, which could explain differences in ligand binding and/or recognition: Phe173 in hVAP-1/Asp in mVAP-1, Leu177/Gln, Asp180/Glu, Val209/Leu, Ser761/Ala, His762/Tyr, and Leu447/Phe from chain B (Figure 4).

The Leu447/Phe substitution could cause problems for the ligand to fit in the rather narrow active site channel of mouse VAP-1, as a phenylalanine is larger and bulkier than a leucine (Figure 4). In the mouse VAP-1 model, Asp173 makes a hydrogen bond to Tyr762, while Phe173 in human VAP-1 can make favorable hydrophobic interactions to the phenyl ring of the inhibitor. Other differences in mouse VAP-1, which are close to the triazole ring of the inhibitor, also account for its less favorable interactions with the inhibitors. The Val209/Leu substitution in mouse VAP-1 model causes the conserved Tyr448B to take an alternative conformation compared to

dx.doi.org/10.1021/jm401372d | *J. Med. Chem.* 2013, 56, 9837−9848

human VAP-1. This altered conformation together with the Asp180/Glu substitution allows hydrogen bonding between Tyr448B and Glu180 in the mouse model, while Tyr448B makes a hydrogen bond to the ligands in the A chain of the human VAP-1 structures (Figure 4). Asp180 always interacts with the triazole group of the pyridazinones in human VAP-1 complexes, whereas the side chain of Glu180 in mouse VAP-1 is longer and cannot form similar interactions. Residues surrounding the methylpiperazinyl and phenyl groups of **13**, which protrudes toward the active site "lip", differ significantly in size and charge between human and mouse VAP-1. Overall, the human protein has more hydrophobic residues (Phe173, Leu177) in this region compared to charged (Asp173) and polar (Gln177) residues in the mouse protein. The effect of Phe173/Asp difference is further increased by the His762/Tyr substitution because in the mouse VAP-1 model Asp173 interacts with Tyr762 whereas the corresponding residues in human VAP-1 are involved in ligand binding. As the studied inhibitors are rather hydrophobic, the human VAP-1 will be more accepting of the inhibitors compared to the rodent protein.

CONCLUSION

In this study, we present a novel set of pyridazinone inhibitors for VAP-1. The synthesized and tested inhibitors show high potency and specificity for human VAP-1 having IC_{50} values from 290 to 20 nM. The inhibitors have excellent specificity over monoamine and diamine oxidases and, moreover, are specific to human and cynomolgus monkey VAP-1 but do not inhibit well the tested rodent VAP-1s. The three determined crystal structures of the inhibitor−VAP-1 complexes confirm a novel binding mode and site in the active site channel for these pyridazinone inhibitors of VAP-1 and reveal that they have ideal binding properties to human VAP-1.

The detailed comparison of their binding mode to human and mouse VAP-1 shows significant differences in the active site channels, which cause the primate specific binding of the studied inhibitors. While the modification of the compounds to improve their binding to rodent VAP-1 may be possible, there are significant challenges associated with this. There are differences between the species throughout the binding site in the active site channel, except for the area in close proximity of TPQ. The Asp180/Glu and Val209/Leu substitutions in mouse VAP-1 seem to cause local rearrangements in binding the triazol group of the inhibitors, which contributes to lower potency in the mouse protein compared to human VAP-1. Similarly, the Phe173/Asp, Leu177/Gln, His762/Tyr, and Leu447B/PheB substitutions contribute to lower potency of inhibitor **13** in mouse VAP-1 compared to human VAP-1 due to less favorable interactions with the second phenyl ring and the piperazine group. Because the differing residues are well distributed in the active site channel and affect the binding of several functional groups of the inhibitors, the design of new pyridazinone derivatives with equal binding properties to human and mouse VAP-1 would be extremely challenging without losing high potency for human VAP-1. An additional disadvantage with this approach is that the significant changes that are required to the compounds in order to improve binding to rodent VAP-1 may introduce unwanted problems with binding specificity, for example, to other copper amine oxidases, or bring toxicological liabilities into the human-specific structures that compromise their further development. Hence, other approaches for the further nonclinical development of human specific VAP-1 agents should be considered. The suitable approaches would include studies with human in vivo transgenic mice models, developing new human disease models, and using existing primate disease models for showing the human VAP-1 inhibitor binding properties.

In summary, these results altogether aid the future development and design of therapeutics for VAP-1 associated diseases. The crystal structures and the characterization of these novel inhibitor molecules enables further development of new pyridazinone derivatives as well as other totally new kinds of reversible human VAP-1 inhibitors. Our results also draw attention to the importance of acknowledging species-specific differences in drug development. Even though these problems can be challenging, they can be solved when the differences are acknowledged, treated appropriately, and future studies conducted accordingly.

EXPERIMENTAL SECTION

Materials. All chemicals were of reagent grade quality or better, obtained from commercial suppliers and used without further purification. Solvents were used as received or dried. Methyl 5-chloro-3-oxo-2-phenyl-2,3-dihydropyridazine-6-carboxylate (**1**),[23] methyl 5-chloro-3-oxo-2-(4-chlorophenyl)-2,3-dihydropyridazine-6-carboxylate (**8**),[24] and 4-(4-methylpiperazin-1-yl)aniline (**9**)[29] were prepared according to the literature procedure. All new compounds whose biological activity was evaluated in this work have a purity ≥98%, as indicated by the elemental analysis data and the ^{1}H NMR spectra.

Instrumentation and Methods. ^{1}H and ^{13}C NMR spectra were recorded in deuterated solvents on 400 (^{1}H, 400 MHz; ^{13}C, 100.6 MHz) MHz spectrometer at room temperature. The chemical shifts, δ, are reported in ppm (parts per million). The residual solvent peaks have been used as an internal reference. Melting points were determined on a Hinotek X-4 type melting point apparatus and are uncorrected. Elemental analyses were performed with a Perkin-Elmer 2400 CHNS elemental analyzer. Merck Kieselgel 60F_{254} plates were used for TLC. The microwave reactions were performed by using CEM LabMate microwave reactor.

Synthesis. *Methyl 3-Oxo-5-phenoxy-2-phenyl-2,3-dihydropyridazine-6-carboxylate (**2**).* A mixture of compound **1** (8.06 g, 30.4 mmol), sodium phenolate trihydrate (5.18 g, 30.4 mmol), and dimethyl formamide (150 mL) was stirred at room temperature for 24 h. The solvent was evaporated in vacuo, and the residue was partitionated between water (200 mL) and EtOAc (200 mL). The organic phase was separated, and the aqueous phase was extracted with EtOAc (2 × 100 mL). The combined organic extracts were washed successively with cold 3% NaOH (2 × 100 mL) and with cold water (2 × 100 mL) and then were dried (Na_2SO_4) and evaporated in vacuo. Et_2O (50 mL) was added to the solid residue, and the crystalline product was filtered off and washed with Et_2O (50 mL). Yield, 7.05 g (72%); mp, 125−126 °C. ^{1}H NMR (400 MHz, $CDCl_3$): δ 3.97 (s, 3H, CH_3), 6.09 (s, 1H, 4-*H*), 7.14−7.19 (m, 2H, Ar), 7.30−7.51 (m, 8H, Ar). ^{13}C NMR (100.6 MHz, $CDCl_3$): δ 53.6, 108.7, 121.5, 126.0, 127.3, 129.1, 129.4, 131.0, 133.8, 141.0, 152.7, 159.4, 161.5, 162.2.

*3-Oxo-5-phenoxy-2-phenyl-2,3-dihydropyridazine-6-carboxamide (**3**).* To a solution of ester **2** (10.00 g, 31 mmol) in MeOH (100 mL), cold 25% methanolic ammonia solution (200 mL) was added. The mixture was stirred at room temperature for 45 min, and then the ammonia was removed at room temperature in vacuo. The solvent was then evaporated at 40−50 °C in vacuo, and the solid residue was dissolved in EtOAc (50 mL). Et_2O (150 mL) was added to the solution, and the separated crystalline product was filtered off and washed with Et_2O (30 mL). Yield, 7.91 g (83%); mp, 177−178 °C. ^{1}H NMR (400 MHz, $CDCl_3$): δ 6.12 (s, 1H, 4-*H*), 6.27 (brs, 1H, NH_2), 6.96 (brs, 1H, NH_2), 7.18−7.22 (m, 2H, Ar), 7.32−7.60 (m, 8H, Ar). ^{13}C NMR (100.6 MHz, $CDCl_3$): δ 109.1, 121.7, 125.9, 127.3, 129.2, 129.4, 131.0, 133.7, 141.0, 152.6, 160.2, 161.6, 163.1.

*N,N-Dimethyl-N′-[(6-oxo-4-phenoxy-1-phenyl-1,6-dihydropyridazin-3-yl)carbonyl]formamidine (**4**).* A mixture of carboxamide **6** (1.45 g, 4.7 mmol) and *N,N*-dimethylformamide dimethyl acetal (2.50 g, 21 mmol) was stirred at 90 °C for 15 min. Then the mixture was cooled down to room temperature, Et_2O (30 mL) was added, and the crystalline product was filtered and washed with Et_2O (2 × 20 mL). Beige crystals; yield, 1.44 g (84%); mp 175−176 °C. ^{1}H NMR (400 MHz, $CDCl_3$) δ 3.22 (s, 3H, NCH_3), 3.24 (s, 3H, NCH_3), 6.13 (s, 1H, 4-*H*), 7.18−7.24 (m, 2H, Ar), 7.29−7.36 (m, 1H, Ar), 7.37−7.43 (m, 1H, Ar), 7.45−7.52 (m, 4H, Ar), 7.60−7.66 (m, 2H, Ar), 8.71 (s, 1H, N=C*H*). ^{13}C NMR (100.6 MHz, $CDCl_3$): δ 36.2, 42.3, 108.8, 121.6, 126.2, 126.9, 128.6, 129.2, 130.8, 140.9, 141.5, 153.1, 159.5, 161.8, 161.9, 173.9.

*5-Phenoxy-2-phenyl-6-(1H-1,2,4-triazol-5-yl)-3(2H)-pyridazinone (**5**).* A mixture of acylamidine **4** (2.75 g, 7.6 mmol), acetic acid (11 mL), and hydrazine hydrate (0.42 g, 8.3 mmol) was stirred at 90 °C for 1.5 h. After the mixture was cooled down to room temperature, Et_2O (30 mL) was added and the mixture was stirred at room temperature for 1 h and then for a further 1 h under ice−water cooling. The crystalline product was filtered off and washed with Et_2O (2 × 15 mL). Yield, 2.23 g (89%); mp, 310−312 °C. ^{1}H NMR (400 MHz, $(CD_3)_2SO$): δ 5.91 (s, 1H, 4-*H*), 7.26−7.61 (m, 10H, Ar) 8.53 (brs, 1H, NC*H*), 14.41 (brs, 1H, N*H*). ^{13}C NMR (100.6 MHz, $(CD_3)_2SO$): δ 108.5, 121.9, 126.7, 127.4, 129.1, 129.6, 131.5, 141.8, 150.1, 153.2, 160.9.

*5-Cyclohexylamino-2-phenyl-6-(1H-1,2,4-triazol-3-yl)-3(2H)-pyridazinone (**6**).* A mixture of compound **5** (1.02 g, 3.1 mmol) and cyclohexylamine (4.5 g) was stirred at 140 °C for 3 h under N_2 atmosphere. The oily mixture was cooled down to room temperature and was crystallized on treatment with Et_2O (50 mL). The crystalline product was filtered off and washed with Et_2O (2 × 25 mL). Yield, 0.80 g (77%). The crude product was recrystallized from a mixture of EtOAc and EtOH; mp, 225−227 °C. ^{1}H NMR (400 MHz, $(CD_3)_2SO$): δ 1.26−1.75 (m, 8H, C_6H_{11}), 1.91−2.00 (m, 2H, C_6H_{11}), 3.45−3.55 (m, 1H, C_6H_{11}), 5.87 (s, 1H, 4-*H*), 7.37−7.42 (1H, m, Ar), 7.46−7.52 (m, 2H, Ar), 7.59−7.67 (m, 2H, Ar), 8.47 (brs, 2H, N*H*, C*H*), 14.70 (brs, 1H, N*H*). ^{13}C NMR (100.6 MHz, $(CD_3)_2SO$): δ 24.5, 26.1, 32.0, 50.4, 96.3, 126.7, 128.3, 129,2, 146.8, 149.4, 155.6, 158.7, 160.6.

*5-Isopropylamino-2-phenyl-6-(1H-1,2,4-triazol-3-yl)-3(2H)-pyridazinone (**7**).* Compound **5** (0.5 g, 1.51 mmol), isopropylamine (2.0 mL), and EtOH (4 mL) were placed in a 10 mL pressurized reaction vial. The mixture was heated by MW irradiation at 150 °C for 60 min. The solvent was then evaporated off, and the residue was crystallized with Et_2O (20 mL) and recrystallized from 15 mL of EtOH/Et_2O (3:2). Yield, 0.35 g (76%); mp, 203−205 °C. ^{1}H NMR (400 MHz, $(CD_3)_2SO$): δ 1.27 (d, 6H, J = 6.3 Hz, CH_3), 3.71−3.77 (m, 1H, C*H*(CH_3)$_2$), 5.83 (s, 1H, 4-*H*), 7.40 (t, 1H, J = 7.3 Hz, Ar), 7.49 (t, 2H, J = 7.6 Hz, Ar), 7.65 (d, 2H, J = 7.3 Hz, Ar), 8.35 (brs, 1H, C*H*), 14.67 (brs, 1H, N*H*). ^{13}C NMR (100.6 MHz, $(CD_3)_2SO$): δ 22.4, 44.0, 96.5, 126.6, 128.3, 129.2, 129.9, 142.2, 146.7, 153.2, 158.2, 160.5.

*Methyl 3-Oxo-5-(4-(4-methylpiperazin-1-yl)phenylamino)-2-(4-chlorophenyl)-2,3-dihydro-pyridazine-6-carboxylate (**10**).* Compound **8** (1.5 g, 5.00 mmol) and **9** (1.0 g, 5.13 mmol) were suspended in EtOH (50 mL) and refluxed. When the TLC showed no more starting material (30 h), the mixture was cooled down to 6−8 °C. The separated crystals were filtered and washed with cold EtOH (2 × 10 mL). Yield, 1.70 g (75%); mp, 164−166 °C. ^{1}H NMR (400 MHz, $CDCl_3$): δ 2.59 (s, 3H, N-CH_3), 2.86−2.94 (m, 4H, CH_3-N-CH_2-CH_2), 3.39−3.46 (m, 4H, CH_3-N-CH_2-CH_2), 3.99 (s, 1H, COOCH_3), 6.13 (s, 1H, 4-*H*), 6.98 (d, 2H, J = 8.8 Hz, Ar), 7.18 (d, 2H, J = 8.7 Hz, Ar), 7.45 (d, 2H, J = 8.8 Hz, Ar), 7.59 (d, 2H, J = 8.8 Hz, Ar), 9.07 (brs, 1H). ^{13}C NMR (100.6 MHz, $CDCl_3$): δ 45.5, 48.6, 53.5, 54.8, 98.9, 117.5, 117.8, 118.6, 126.5, 127.2, 129.3, 129.7, 134.5, 140.1, 148.5, 149.6, 161.2.

*3-Oxo-5-(4-(4-methylpiperazin-1-yl)phenylamino)-2-(4-chlorophenyl)-2,3-dihydro-pyridazine-6-carboxamide (**11**).* The mixture of **10** (1.3 g, 2.86 mmol), MeOH (20 mL), and 25% methanolic ammonia solution (10 mL) was placed in a dark bottle, shaken carefully 2 times, and allowed to stand overnight. The solvent was then removed, and the residue was crystallized from EtOH/Et_2O (5:40 mL). Yield, 1.16 g (92%); mp, 183−185 °C. ^{1}H NMR (400 MHz, $(CD_3)_2SO$): δ 2.81 (s, 3H, N-CH_3), 3.12−3.33 (m, 4H, CH_3-N-CH_2-CH_2), 3.42−3.91 (m, 4H, CH_3-N-CH_2-CH_2), 5.85 (s, 1H, 4-*H*), 7.08 (d, 2H, J = 8.8 Hz, Ar), 7.23 (d, 2H, J = 8.6 Hz, Ar), 7.53 (d, 2H, J = 8.7 Hz, Ar), 7.73 (d, 2H, J = 8.6 Hz, Ar), 7.96 (brs, 1H, NH_2), 8.17 (brs, 1H, NH_2), 10.08 (brs, 1H, N*H*). ^{13}C NMR (100.6 MHz, $(CD_3)_2SO$): δ 42.8, 46.3, 52.8, 97.6, 117.8, 125.8, 128.2, 129.1, 129.5, 130.3, 132.9, 140.5, 148.2, 148.3, 160.6, 167.6.

*N,N-Dimethyl-N′-[(6-oxo-4-(4-methylpiperazin-1-yl)phenylamino)-1-(4-chlorophenyl)-1,6-dihydropyridazin-3-yl)carbonyl]formamidine (**12**).* The carboxamide **11** (1.1 g, 2.51 mmol) was suspended in *N,N*-dimethylformamide dimethyl acetal (6 mL) and stirred for 30 min at rt. Then Et_2O (25 mL) was added. The precipitate was filtered off and washed with Et_2O (2 × 10 mL). Yield, 1.15 g (93%); mp, 112−115 °C. ^{1}H NMR (400 MHz, $(CD_3)_2SO$): δ 2.24 (s, 3H, N-CH_3), 2.43−2.49 (m, 4H, CH_3-N-CH_2-CH_2), 3.07−3.31 (m, 10H, CH_3-N-CH_2-CH_2, N-(CH_3)$_2$), 5.84 (s, 1H, 4-*H*), 7.01 (d, 2H, J = 8.0 Hz, Ar), 7.18 (d, 2H, J = 8.3 Hz, Ar), 7.55 (d, 2H, J = 8.333 Hz, Ar), 7.61 (d, 2H, J = 8.6 Hz, Ar), 8.72 (s, 1H, N=CH), 10.57 (brs, 1H, N*H*). ^{13}C NMR (100.6 MHz, $(CD_3)_2SO$): δ 36.7, 42.4, 46.6, 48.9, 55.4, 96.8, 117.1, 125.5, 128.2, 129.3, 129.5, 132.8, 134.3, 141.2, 148.6, 149.7, 161.7.

*5-(4-(4-Methylpiperazin-1-yl)phenylamino)-2-(4-chlorophenyl)-6-(1H-1,2,4-triazol-3-yl)-3(2H)-pyridazinone Hydrochloride (**13**).* Compound **12** (1.0 g, 2.02 mmol) was dissolved in acetic acid (5 mL). Hydrazine hydrate (0.1 g, 2.0 mmol) was added, and the mixture was stirred at 80 °C for 1.5 h. The solvent was removed under reduced pressure, and the residue crystallized from Et_2O (20 mL). The crystals was filtered and washed with Et_2O (2 × 5 mL), with 1 M sodium carbonate solution (2 × 15 mL), and with water (3 × 20 mL). Yield: (the free base), 0.83 g (89%); mp, 203−205 °C.

Isolation of the hydrochloric salt of the target compound:

The free base of **13** (0.5 g, 1.08 mmol) was suspended in EtOH (5 mL) and then 50 μL of ethanolic hydrochloric acid solution (22%) was added. The mixture was stirred for 0.5 h, and then Et_2O (15 mL) was added. The precipitate was filtered, washed with Et_2O (2 × 10 mL), and recrystallized from 20 mL of EtOH/Et_2O (5:15); mp, 221−223 °C. ^{1}H NMR (400 MHz, $(CD_3)_2SO$): δ 2.82 (s, 3H, N-CH_3), 3.11−3.22 (m, 4H, CH_3-N-CH_2-CH_2), 3.46−3.90 (m, 4H, CH_3-N-CH_2-CH_2), 5.93 (s, 1H, 4-*H*), 7.11 (d, 2H, J = 8.7 Hz, Ar), 7.29 (d, 2H, J = 8.6 Hz, Ar), 7.56 (d, 2H, J = 8.8 Hz, Ar), 7.74 (d, 2H, J = 8.6 Hz, Ar), 8.56 (brs, 1H, C*H*), 10.00 (brs, 1H, N*H*), 11.05 (brs, 1H, N*H*), 14.92 (brs, 1H, N*H*). ^{13}C NMR (100.6 MHz, $(CD_3)_2SO$): δ 42.8, 46.3, 52.9, 98.0, 117.8, 126.1, 128.1, 129.2, 130.4, 132.7, 140.8, 148.5, 160.4.

Expression of Recombinant VAP-1. Recombinant human VAP-1 protein was obtained from Chinese hamster ovary (CHO) cells stably transfected with a full-length human VAP-1 cDNA. Recombinant human VAP-1 SSAO expressed in CHO cells was used as a source of VAP-1 for activity measurements. Native CHO cells have negligible VAP-1 activity. These cells and their culture have previously been described.[3] A cell lysate was prepared as described previously.[37] The corresponding recombinant mouse VAP-1 and cynomolgus monkey VAP-1 proteins were obtained from Chinese hamster ovary (CHO) cells stably transfected with a full-length mouse VAP-1 cDNA as described above.[3]

Mitochondrial MAO Extract. Rat total monoamine oxidase enzyme (MAO, mixture of MAO A and MAO B) was prepared from rat liver tissues, homogenized and isolated as described previously.[30] Purified human MAO A and MAO B were purchased from Sigma-Aldrich.

In Vitro Inhibition of VAP-1 Activity. VAP-1 activity was measured as described previously using the coupled colorimetric method as described for monoamine oxidase and related enzymes.[30,37,41] In short, the assay was performed in 96-well microtiter plates as follows. The inhibitor concentration used varied between 1 nM and 50 μM. The assay was performed in a final volume of 200 μL consisting of 0.2 M potassium phosphate buffer (pH 7.6) and freshly made chromogenic solution containing 1 mM 2,4-dichlorophenol, 500 μM 4-aminoantipyrine, and 4 U/mL horseradish peroxidase and an amount of CHO cell lysate containing VAP-1 SSAO that caused a change of 0.6 A^{490} per h. This was within the linear response range of

Table 2. Crystallographic Data Collection and Refinement Statistics for the VAP-1 Complexes with Inhibitors 6, 7, and 13

	6−VAP-1	7−VAP-1	13−VAP-1
Data Collection			
space group	$P6_522$	$P6_522$	$P6_522$
cell dimensions (Å)	$a = b = 226.47$, $c = 219.25$	$a = b = 226.35$, $c = 217.23$	$a = b = 226.73$, $c = 218.16$
resolution (Å)[a]	50−2.8 (2.85−2.80)	50−2.78 (2.83−2.78)	50−3.10 (3.15−3.10)
R_{merge}[b](%)	30.1 (n/a)[c]	17.8 (n/a)[c]	29.9 (n/a)[c]
$\langle I\rangle/\langle\sigma I\rangle$	1.7[d]	19.2[d]	4.6[d]
completeness (%)	95.8 (82.6)	99.8 (98.4)	99.3 (96.4)
redundancy	9.0 (5.8)	6.9 (5.3)	5.7 (3.9)
$CC_{1/2}$	0.110	0.520	0.229
Refinement			
resolution (Å)	49.40−2.80	49.00−2.78	49.20−3.10
no. reflns	60329	62917	43449
R_{factor}/R_{free} (%)	20.7/26.0	18.1/24.0	18.3/24.8
Wilson *B*-value	53	45	86
no. atoms:			
protein	11137	11126	11143
ligand	25	22	33
water	106	296	40
B-factor (Å^2)			
protein	62	40	87
ligand	80	39	88
water	44	27	54
rms deviation			
bond length (Å)	0.01	0.01	0.01
bond angle (deg)	1.7	1.7	1.8

[a]Values in parentheses are for highest resolution shells, where applicable. [b]$R_{merge} = \sum_{hkl}\sum_i |I_i(hkl) - \langle I(hkl)\rangle|/\sum_{hkl}\sum_i I_i(hkl)$, where I runs over multiple observations of the same intensity and *hkl* runs over all crystallography unique intensities. [c]If R_{merge} exceeds 1.0, Scalepack does not report its value because it is uninformative. [d]Anisotropic diffraction; $\langle I\rangle/\langle\sigma I\rangle$ for highest resolution shells in complexes **6** (x and y 1.75, z 0.75, and z 1.0 at 3.54 Å), **7** (x and y 3.5, z 0.17, and z 1.0 at 3.5 Å), and **13** (x and y 2.68, z 0.27, and z 1.2 at 3.58 Å). Data were cut elliptically in Scalepack to correct for anisotropy. Diffraction data for **6**−VAP-1 complex was acquired with Pilatus detector at ESRF ID29 beamline with very low dose per image. This is the reason why the average intensity for the data set is low. Nevertheless, molecular refinement statistics and omit electron density maps have the features typical for the resolution of the data and R_{factor} and R_{free} values in the highest resolution shell in refinement indicates that the selected resolution cuts have not been overly optimistic.

the assay. The plates were incubated for 30 min at 37 °C. To initiate the enzyme reaction, 1 mM benzylamine as a final concentration was added and the plate incubated for 1 h at 37 °C. The increase in absorbance, reflecting VAP-1 SSAO activity, was measured at 490 nm by using a Wallac Victor II multilabel counter. Inhibition was presented as percent inhibition compared to control after correcting for background absorbance and IC_{50} values calculated using GraphPad Prism software. Monoamine oxidase (MAO) activities were measured in a similar way as for VAP-1 SSAO except that 2,4-dichlorophenol was replaced by 1 mM vanillic acid, and benzylamine was replaced by tyramine at 0.5 mM final concentration.

Biacore T100 instrument was used to analyze the binding kinetics of compounds **6** and **7** to VAP-1 protein. Recombinant purified VAP-1 was amine coupled to a CM5 sensor chip. It was preconcentrated in 10 mM NaAcetate pH 4.4 with 10 μM $CuCl_2$. The compounds were tested in 25 mM Tris pH 7.4, 150 mM NaCl, 10 μM $CuCl_2$, 5% DMSO, and 0.005% Tween-20 at 25 °C. Compounds were tested in a 3-fold dilution series.

Extraction and Purification of Serum VAP-1 for Crystallization. The soluble form of VAP-1 was extracted and purified from human serum by Biotie Therapies Corp. The human serum sample was first prefiltered, concentrated, and purified as previously described for recombinant VAP-1[42] and finally dialyzed against 10 mM potassium phosphate (pH 7.2). The protein was concentrated to approximately 1.0 mg/mL and used for crystallization.

Crystallization and Diffraction Data Collection. Crystallization experiments were performed at room temperature using the hanging drop vapor diffusion method. The protein was incubated with the inhibitors for 1 h at 37° in a 1:10 protein to inhibitor molar ratio prior to crystallization setup. For crystallization, 1 μL of the protein inhibitor sample was mixed with 1 μL of well solution containing 0.6−0.75 M Na/K tartrate, 0.2 M NaCl, 0.1 M Hepes, pH 7.4−7.6. The crystals grew slowly, and at the moment of the data collection they had been growing for 11 months. Prior to data collection, the crystals were soaked for 10 s in a cryoprotectant containing 0.7−0.8 M Na/K tartrate, 0.2 M NaCl, 0.1 M Hepes, pH 7.6, 1.3−1.57 M Naformate, 0.05 mM inhibitor, and cryocooled in liquid nitrogen. Data collection was carried out at the European Synchrotron Radiation Facility (ESRF) at beamline ID23−2 on a MAR225 CCD detector for the **7** and **13** complexes, while the **6**−VAP-1 complex data were collected at beamline ID29 on a Pilatus 6 M detector.

Data Processing, Structure Solution, and Refinement. Diffraction data were indexed, integrated, scaled, and processed with HKL3000[43] in space group $P6_522$. The structures were solved with molecular replacement within the CCP4i program suite[44] with the dimer of human VAP-1 structure (PDB code 1US1) as the search model.

All crystals showed significant anisotropy. The VAP-1−**6** complex crystal diffracted to a resolution of 3.0 Å. The indexing of the crystal lattice was challenging due to the very low number of counts in the diffraction peaks, resulting in a signal-to-noise ratio of ∼0.1 calculated over all of the Bragg peaks in the diffraction image. Even though the Pilatus 6 M detector has virtually no readout noise, the identification of peaks requires a signal-to-noise ratio above 5 for a number of diffraction peaks large enough to run the autoindexing algorithm. Therefore, for autoindexing to work, we decreased the default threshold for the peak search procedure and performed it on multiple, consecutive frames, which is not a default option in HKL3000.[43,45]

During the data processing of all crystals, we applied computational corrections for absorption in a crystal and imprecise calculations of the

dx.doi.org/10.1021/jm401372d | J. Med. Chem. 2013, 56, 9837−9848

Lorentz factor resulting from a minor misalignment of the goniostat.[46,47] We also used the procedure to correct for anisotropic diffraction, to adjust the error model, and to adjust the phasing signal to compensate for a radiation-induced increase of nonisomorphism within the crystal.[48−50] While all of these corrections were important for successful data processing, correcting for anisotropic diffraction was particularly important for the quality of the final electron density maps because along the 6-fold axis the diffraction was attenuated by a *B*-factor of 54 Å^2 relative to the diffraction in the perpendicular directions. This resulted in an effective resolution of ∼3.9 Å along the 6-fold axis, while the resolution along the perpendicular directions was better than 3.0 Å. The data statistics are presented in Table 2.

A dimer, one biological unit, was located in the asymmetric unit of all structures. The models were first refined as a rigid body with REFMAC5.[51] The models were rebuilt using COOT[52] followed by multiple rounds of restrained refinement with REFMAC5. The three-dimensional structures and restraints dictionaries for the inhibitors were made in the online PRODRG Sever.[53] Stereochemical quality of the structures was assessed with Molprobity[54] and Moleman.[55,56]

Structure Analysis and Visualization. COOT,[52] Maestro,[57] Sfcheck,[58] and Pymol[59] were used to analyze, visualize, and inspect the structures. Pymol was used to make the figures.

Modeling of Mammalian VAP-1s in Complex with Inhibitor 13. The modeling of mouse, and cynomolgus monkey VAP-1 was done as previously described.[42] The complex structure of sVAP-1 and inhibitor **13** was used as the template structure.

■ ASSOCIATED CONTENT

Ⓢ Supporting Information

NMR spectra of compounds **2**−**13**. Electron density maps for active site, glycosylation, and omit map of the **13**−VAP-1 complex structure. This material is available free of charge via the Internet at http://pubs.acs.org.

Accession Codes

Coordinates and structure factors are deposited at the Protein Data Bank with codes 4bty, 4btx, and 4btw.

■ AUTHOR INFORMATION

Corresponding Author

*Phone: +35822154003. Fax: +35822153280. E-mail: tiina.salminen@abo.fi.

Notes

The authors declare no competing financial interest.

■ ACKNOWLEDGMENTS

This work was supported by the National Programme in Informational and Structural Biology (E.B.), Sigrid Juselius Foundation (T.A.S), the Tor, Joe, and Pentti Borgs Foundation (E.B. and T.A.S.), Medicinska Understödsföreningen Liv och hälsa (T.A.S. and E.B), and the Academy of Finland (132998; T.A.S), and Prof. Mark Johnson for the excellent computing facilities at Åbo Akademi University. Use of Biocenter Finland infrastructure at Åbo Akademi (bioinformatics, structural biology, and translational activities) is acknowledged. Dr. Dominika Borek is acknowledged for assistance in data processing, and the APS/CCP4 workshop is acknowledged for arranging an outstanding workshop on data collection and structural determination. We also thank the European Synchrotron Radiation Facility for provision of synchrotron radiation facilities.

■ ABBREVIATIONS USED

VAP-1, vascular adhesion protein-1; SSAO, semicarbazide-sensitive amine oxidases; CAO, copper-containing amine oxidase; TPQ, topaquinone; DAO, diamine oxidase; MAO, monoamine oxidase; CCR2, CC chemokine receptor 2; CCL2, CC chemokine ligand 2; CCR5, CC chemokine receptor 5; TLC, thin layer chromatography

■ REFERENCES

(1) Palfreyman, M. G.; McDonald, I. A.; Bey, P.; Danzin, C.; Zreika, M.; Cremer, G. Haloallylamine inhibitors of MAO and SSAO and their therapeutic potential. *J. Neural Transm. Suppl.* **1994**, *41*, 407−414.

(2) Floris, G. *Copper Amine Oxidases: Structures, Catalytic Mechanisms, And Role in Pathophysiology*; CRC Press: Boca Raton, FL, 2009; p 344.

(3) Smith, D. J.; Salmi, M.; Bono, P.; Hellman, J.; Leu, T.; Jalkanen, S. Cloning of vascular adhesion protein 1 reveals a novel multifunctional adhesion molecule. *J. Exp. Med.* **1998**, *188*, 17−27.

(4) Salmi, M.; Jalkanen, S. VAP-1: an adhesin and an enzyme. *Trends Immunol.* **2001**, *22*, 211−216.

(5) Salmi, M.; Jalkanen, S. Ectoenzymes controlling leukocyte traffic. *Eur. J. Immunol.* **2012**, *42*, 284−292.

(6) Dunkel, P.; Balogh, B.; Meleddu, R.; Maccioni, E.; Gyires, K.; Matyus, P. Semicarbazide-sensitive amine oxidase/vascular adhesion protein-1: a patent survey. *Expert Opin. Ther. Pat.* **2011**, *21*, 1453−1471.

(7) Parsons, M. R.; Convery, M. A.; Wilmot, C. M.; Yadav, K. D.; Blakeley, V.; Corner, A. S.; Phillips, S. E.; McPherson, M. J.; Knowles, P. F. Crystal structure of a quinoenzyme: copper amine oxidase of *Escherichia coli* at 2 A resolution. *Structure* **1995**, *3*, 1171−1184.

(8) Wilce, M. C.; Dooley, D. M.; Freeman, H. C.; Guss, J. M.; Matsunami, H.; McIntire, W. S.; Ruggiero, C. E.; Tanizawa, K.; Yamaguchi, H. Crystal structures of the copper-containing amine oxidase from *Arthrobacter globiformis* in the holo and apo forms: implications for the biogenesis of topaquinone. *Biochemistry* **1997**, *36*, 16116−16133.

(9) Li, R.; Chen, L.; Cai, D.; Klinman, J. P.; Mathews, F. S. Crystallographic study of yeast copper amine oxidase. *Acta Crystallogr., Sect. D: Biol. Crystallogr.* **1997**, *53*, 364−370.

(10) Duff, A. P.; Cohen, A. E.; Ellis, P. J.; Kuchar, J. A.; Langley, D. B.; Shepard, E. M.; Dooley, D. M.; Freeman, H. C.; Guss, J. M. The crystal structure of *Pichia pastoris* lysyl oxidase. *Biochemistry* **2003**, *42*, 15148−15157.

(11) McGrath, A. P.; Mithieux, S. M.; Collyer, C. A.; Bakhuis, J. G.; van den Berg, M.; Sein, A.; Heinz, A.; Schmelzer, C.; Weiss, A. S.; Guss, J. M. Structure and activity of *Aspergillus nidulans* copper amine oxidase. *Biochemistry* **2011**, *50*, 5718−5730.

(12) Freeman, H. C.; Guss, J. M.; Kumar, V.; McIntire, W. S.; Zubak, V. M. Purification, crystallization and preliminary X-ray crystal structure analysis of copper amine oxidase from *Arthrobacter globoformis*. *Acta Crystallogr., Sect. D: Biol. Crystallogr.* **1996**, *52*, 197−198.

(13) Airenne, T. T.; Nymalm, Y.; Kidron, H.; Smith, D. J.; Pihlavisto, M.; Salmi, M.; Jalkanen, S.; Johnson, M. S.; Salminen, T. A. Crystal structure of the human vascular adhesion protein-1: unique structural features with functional implications. *Protein Sci.* **2005**, *14*, 1964−1974.

(14) Jakobsson, E.; Nilsson, J.; Ogg, D.; Kleywegt, G. J. Structure of human semicarbazide-sensitive amine oxidase/vascular adhesion protein-1. *Acta Crystallogr., Sect. D: Biol. Crystallogr.* **2005**, *61*, 1550−1562.

(15) Ernberg, K.; McGrath, A. P.; Peat, T. S.; Adams, T. E.; Xiao, X.; Pham, T.; Newman, J.; McDonald, I. A.; Collyer, C. A.; Guss, J. M. A new crystal form of human vascular adhesion protein 1. *Acta Crystallogr., Sect. F: Struct. Biol. Cryst. Commun.* **2010**, *66*, 1572−1578.

(16) Lunelli, M.; Di Paolo, M. L.; Biadene, M.; Calderone, V.; Battistutta, R.; Scarpa, M.; Rigo, A.; Zanotti, G. Crystal structure of amine oxidase from bovine serum. *J. Mol. Biol.* **2005**, *346*, 991−1004.

(17) Holt, A.; Smith, D. J.; Cendron, L.; Zanotti, G.; Rigo, A.; Di Paolo, M. L. Multiple binding sites for substrates and modulators of semicarbazide-sensitive amine oxidases: kinetic consequences. *Mol. Pharmacol.* **2008**, *73*, 525−538.

(18) Elovaara, H.; Kidron, H.; Parkash, V.; Nymalm, Y.; Bligt, E.; Ollikka, P.; Smith, D. J.; Pihlavisto, M.; Salmi, M.; Jalkanen, S.; Salminen, T. A. Identification of two imidazole binding sites and key residues for substrate specificity in human primary amine oxidase AOC3. *Biochemistry* **2011**, *50*, 5507−5520.
(19) Emanuela, B.; Minarini, A.; Tumiatti, V.; Milelli, A.; Lunelli, M.; Pegoraro, M.; Rizzoli, V.; Di Paolo, M. L. Synthetic polyamines as potential amine oxidase inhibitors: a preliminary study. *Amino Acids* **2012**, *42*, 913−928.
(20) Foot, J. S.; Deodhar, M.; Turner, C. I.; Yin, P.; van Dam, E. M.; Silva, D. G.; Olivieri, A.; Holt, A.; McDonald, I. A. The discovery and development of selective 3-fluoro-4-aryloxyallylamine inhibitors of the amine oxidase activity of semicarbazide-sensitive amine oxidase/vascular adhesion protein-1 (SSAO/VAP-1). *Bioorg. Med. Chem. Lett.* **2012**, *22*, 3935−3940.
(21) Yu, P. H.; Zuo, D. M.; Davis, B. A. Characterization of human serum and umbilical artery semicarbazide-sensitive amine oxidase (SSAO). Species heterogeneity and stereoisomeric specificity. *Biochem. Pharmacol.* **1994**, *47*, 1055−1059.
(22) Marti, L.; Abella, A.; De La Cruz, X.; Garcia-Vicente, S.; Unzeta, M.; Carpene, C.; Palacin, M.; Testar, X.; Orozco, M.; Zorzano, A. Exploring the binding mode of semicarbazide-sensitive amine oxidase/VAP-1: identification of novel substrates with insulin-like activity. *J. Med. Chem.* **2004**, *47*, 4865−4874.
(23) Schober, B. D.; Megyeri, G.; Kappe, T. Pyridazines with heteroatom substituents in position 3 and 5. 3. 2-Aryl-5-hydroxypyridazin-3(2*H*)-ones as potential herbicides: Synthesis and some reactions. *J. Heterocycl. Chem* **1989**, *26*, 169−176.
(24) Schober, B. D.; Megyeri, G.; Kappe, T. Pyridazines with heteroatom substituents in positions 3 and 5. 6. S−N reactions in position 5 of 2-aryl-5-hydroxypyridazin-3(2*H*)-ones. *J. Heterocycl. Chem.* **1990**, *27*, 471−477.
(25) Dajka-Halasz, B.; Monsieurs, K.; Élias, O.; Károlyházy, L.; Tapolcsányi, P.; Maes, B. U. W.; Riedl, Z.; Hajós, G.; Dommisse, R. A.; Lemière, G. L. F.; Kosmrlj, J.; Mátyus, P. Synthesis of 5*H*-pyridazino4,5-*b*]indoles and their benzofurane analogues utilizing an intramolecular Heck-type reaction. *Tetrahedron* **2004**, *60*, 2283.
(26) Lin, Y.; Lang, S. A.; Lovell, M. F.; Perkinson, N. A. New synthesis of 1,2,4-triazoles and 1,2,4-oxadiazoles. *J. Org. Chem.* **1979**, *44*, 4160−4164.
(27) Marlow, A. L.; Wallace, E.; Seo, J.; Lyssikatos, J. P.; Yang, H.; Blake, J. Heterocyclic inhibitors of MEK and methods of use thereof. S20050256123, 2005.
(28) Marlow, A. L.; Wallace, E.; Seo, J.; Lyssikatos, J. P.; Yang, H. W.; Blake, J.; Storey, R.; Booth, R. J.; Pittam, J. D.; Leonard, J.; Fielding, M. R. Heterocyclic inhibitors of MEK and methods of use thereof. WO2007044084, 2007.
(29) Meegalla, S. K.; Wall, M. J.; Chen, J.; Wilson, K. J.; Ballentine, S. K.; DesJarlais, R. L.; Schubert, C.; Crysler, C. S.; Chen, Y.; Molloy, C. J.; Chaikin, M. A.; Manthey, C. L.; Player, M. R.; Tomczuk, B. E.; Illig, C. L. Structure-based optimization of a potent class of arylamide FMS inhibitors. *Bioorg. Med. Chem. Lett.* **2008**, *18*, 3632−3637.
(30) Nurminen, E. M.; Pihlavisto, M.; Lazar, L.; Pentikainen, U.; Fulop, F.; Pentikainen, O. T. Novel hydrazine molecules as tools to understand the flexibility of vascular adhesion protein-1 ligand-binding site: toward more selective inhibitors. *J. Med. Chem.* **2011**, *54*, 2143−2154.
(31) Bligt-Linden, E.; Arunachalam, R.; Parkash, V.; Salminen, T. A. Structural comparison of the active site channels in rodent and primate vascular adhesion protein-1. *J. Neural Transm.* **2013**, *120*, 947−950.
(32) Yraola, F.; Garcia-Vicente, S.; Fernandez-Recio, J.; Albericio, F.; Zorzano, A.; Marti, L.; Royo, M. New efficient substrates for semicarbazide-sensitive amine oxidase/VAP-1 enzyme: analysis by SARs and computational docking. *J. Med. Chem.* **2006**, *49*, 6197−6208.
(33) Peltz, G. Can 'humanized' mice improve drug development in the 21st century? *Trends Pharmacol. Sci.* **2013**, *34*, 255−260.
(34) Misharin, A. V.; Haines, G. K., III; Rose, S.; Gierut, A. K.; Hotchkiss, R. S.; Perlman, H. Development of a new humanized mouse model to study acute inflammatory arthritis. *J. Transl. Med.* **2012**, *10*, 190.
(35) Imam, S.; Elagin, R. B.; Jaume, J. C. Diabetes-associated dry eye syndrome in a new humanized transgenic model of type 1 diabetes. *Mol. Vis.* **2013**, *19*, 1259−1267.
(36) Maula, S. M.; Salminen, T.; Kaitaniemi, S.; Nymalm, Y.; Smith, D. J.; Jalkanen, S. Carbohydrates located on the top of the "cap" contribute to the adhesive and enzymatic functions of vascular adhesion protein-1. *Eur. J. Immunol.* **2005**, *35*, 2718−2727.
(37) Nurminen, E. M.; Pihlavisto, M.; Lazar, L.; Szakonyi, Z.; Pentikainen, U.; Fulop, F.; Pentikainen, O. T. Synthesis, in vitro activity, and three-dimensional quantitative structure−activity relationship of novel hydrazine inhibitors of human vascular adhesion protein-1. *J. Med. Chem.* **2010**, *53*, 6301−6315.
(38) Inoue, T.; Morita, M.; Tojo, T.; Yoshihara, K.; Nagashima, A.; Moritomo, A.; Ohkubo, M.; Miyake, H. Synthesis and SAR study of new thiazole derivatives as vascular adhesion protein-1 (VAP-1) inhibitors for the treatment of diabetic macular edema. *Bioorg. Med. Chem.* **2013**, *21*, 1219−1233.
(39) Inoue, T.; Morita, M.; Tojo, T.; Nagashima, A.; Moritomo, A.; Imai, K.; Miyake, H. Synthesis and SAR study of new thiazole derivatives as vascular adhesion protein-1 (VAP-1) inhibitors for the treatment of diabetic macular edema: part 2. *Bioorg. Med. Chem.* **2013**, *21*, 2478−2494.
(40) McGrath, A. P.; Hilmer, K. M.; Collyer, C. A.; Shepard, E. M.; Elmore, B. O.; Brown, D. E.; Dooley, D. M.; Guss, J. M. Structure and inhibition of human diamine oxidase. *Biochemistry* **2009**, *48*, 9810−9822.
(41) Holt, A.; Sharman, D. F.; Baker, G. B.; Palcic, M. M. A continuous spectrophotometric assay for monoamine oxidase and related enzymes in tissue homogenates. *Anal. Biochem.* **1997**, *244*, 384−392.
(42) Nymalm, Y.; Kidron, H.; Soderholm, A.; Viitanen, L.; Kaukonen, K.; Pihlavisto, M.; Smith, D.; Veromaa, T.; Airenne, T. T.; Johnson, M. S.; Salminen, T. A. Crystallization and preliminary X-ray analysis of the human vascular adhesion protein-1. *Acta Crystallogr., Sect. D: Biol. Crystallogr.* **2003**, *59*, 1288−1290.
(43) Otwinowski, Z.; Minor, W. Processing of X-ray diffraction data collected in the oscillation mode. *Method Enzymol.* **1997**, *276*, 307−326.
(44) Dodson, E. J.; Winn, M.; Ralph, A. Collaborative Computational Project, number 4: providing programs for protein crystallography. *Methods Enzymol.* **1997**, *277*, 620−633.
(45) Minor, W.; Cymborowski, M.; Otwinowski, Z.; Chruszcz, M. HKL-3000: the integration of data reduction and structure solution—from diffraction images to an initial model in minutes. *Acta Crystallogr., Sect. D: Biol. Crystallogr.* **2006**, *62*, 859−866.
(46) Borek, D.; Minor, W.; Otwinowski, Z. Measurement errors and their consequences in protein crystallography. *Acta Crystallogr., Sect. D: Biol. Crystallogr.* **2003**, *59*, 2031−2038.
(47) Otwinowski, Z.; Borek, D.; Majewski, W.; Minor, W. Multiparametric scaling of diffraction intensities. *Acta Crystallogr., Sect. A: Found. Crystallogr.* **2003**, *59*, 228−234.
(48) Borek, D.; Cymborowski, M.; Machius, M.; Minor, W.; Otwinowski, Z. Diffraction data analysis in the presence of radiation damage. *Acta Crystallogr., Sect. D: Biol. Crystallogr.* **2010**, *66*, 426−436.
(49) Borek, D.; Ginell, S. L.; Cymborowski, M.; Minor, W.; Otwinowski, Z. The many faces of radiation-induced changes. *J. Synchrotron Radiat.* **2007**, *14*, 24−33.
(50) Borek, D.; Dauter, Z.; Otwinowski, Z. Identification of patterns in diffraction intensities affected by radiation exposure. *J. Synchrotron Radiat.* **2013**, *20*, 37−48.
(51) Murshudov, G. N.; Vagin, A. A.; Dodson, E. J. Refinement of macromolecular structures by the maximum-likelihood method. *Acta Crystallogr., Sect. D: Biol. Crystallogr.* **1997**, *53*, 240−255.
(52) Emsley, P.; Cowtan, K. Coot: model-building tools for molecular graphics. *Acta Crystallogr., Sect. D: Biol. Crystallogr.* **2004**, *60*, 2126−2132.

(53) Schuttelkopf, A. W.; van Aalten, D. M. PRODRG: a tool for high-throughput crystallography of protein−ligand complexes. *Acta Crystallogr., Sect. D: Biol. Crystallogr.* **2004**, *60*, 1355−1363.
(54) Davis, I. W.; Leaver-Fay, A.; Chen, V. B.; Block, J. N.; Kapral, G. J.; Wang, X.; Murray, L. W.; Arendall, W. B., III; Snoeyink, J.; Richardson, J. S.; Richardson, D. C. MolProbity: all-atom contacts and structure validation for proteins and nucleic acids. *Nucleic Acids Res.* **2007**, *35*, W375−W383.
(55) Kleywegt, G. J. Unpublished program. Uppsala University: Uppsala, Sweden, 1992−2001.
(56) Kleywegt, G. J.; Zou, J. Y.; Kjeldgaard, M.; Jones, T. A. Model Building and Computer Graphics. In *International Tables for Crystallography, Vol. F: Crystallography of Biological Macromolecules*; Rossman, M. G., Arnold, E., Eds.; Kluwer Academic Publishers: Dordrecht, The Netherlands, 2001; pp 353−356, 366−367.
(57) *Maestro*, v. 9.3; Schrödinger, LLC: New York,, 2012.
(58) Vagin, A. A.; Richelle, J.; Wodak, S. J. SFCHECK: a unified set of procedure for evaluating the quality of macromolecular structure-factor data and their agreement with atomic model. *Acta Cryst.* **1999**, *D55*, 191−205.
(59) DeLano, W. L. *The PyMoL Molecular Graphics Systems.* Scientific LLC: Palo Alto, CA, 2008.